

# SpectralEarth: Training Hyperspectral Foundation Models at Scale

Nassim Ait Ali Braham<sup>1,2</sup>

Conrad M Albrecht<sup>2</sup>  
Yi Wang<sup>1</sup>

Julien Mairal<sup>3</sup>  
Xiao Xiang Zhu<sup>1</sup>

Jocelyn Chanussot<sup>3</sup>

<sup>1</sup>Data Science in Earth Observation, Technical University of Munich, Germany

<sup>2</sup>Remote Sensing Technology Institute, German Aerospace Center, Germany

<sup>3</sup>Univ. Grenoble Alpes, Inria, CNRS, Grenoble INP, LJK, 38000 Grenoble, France

## Abstract

Foundation models have triggered a paradigm shift in computer vision and are increasingly being adopted in remote sensing, particularly for multispectral imagery. Yet, their potential in hyperspectral imaging (HSI) remains untapped due to the absence of comprehensive and globally representative hyperspectral datasets. To close this gap, we introduce SpectralEarth, a large-scale multi-temporal dataset designed to pretrain hyperspectral foundation models leveraging data from the Environmental Mapping and Analysis Program (EnMAP). SpectralEarth comprises 538,974 image patches covering 415,153 unique locations from more than 11,636 globally distributed EnMAP scenes spanning two years of archive. Additionally, 17.5% of these locations include multiple timestamps, enabling multi-temporal HSI analysis. Utilizing state-of-the-art self-supervised learning (SSL) algorithms, we pretrain a series of foundation models on SpectralEarth. We integrate a spectral adapter into classical vision backbones to accommodate the unique characteristics of HSI. In tandem, we construct four downstream datasets for land-cover and crop-type mapping, providing benchmarks for model evaluation. Experimental results support the versatility of our models, showcasing their generalizability across different tasks and sensors. We also highlight computational efficiency during model fine-tuning. The dataset, models, and source code will be made publicly available.

## 1. Introduction

Hyperspectral imaging (HSI) from space provides valuable information about the material composition of the Earth’s surface and atmosphere. With hundreds of narrow bands, each a few nanometers in width, hyperspectral images record detailed electromagnetic information across a wide range of wavelengths, from long-wave ultraviolet

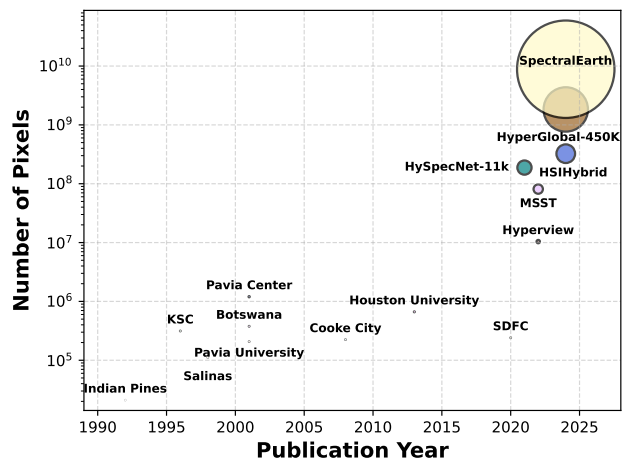


Figure 1. Visualization of scale for various hyperspectral datasets published within the past three decades. The plot serves to illustrate the volume of the SpectralEarth dataset (area of circles).

to the shortwave infrared [39]. This rich spectral information provides opportunities for numerous environmental applications such as soil and mineral mapping, pollution tracking, agricultural assessment, and forest monitoring [13, 35, 45, 61, 62].

In recent years, the availability of hyperspectral data has been significantly expanded by the launch of new satellite missions. Notable examples include: Germany’s Environmental Mapping and Analysis Program (EnMAP) [37] with precursor Earth Sensing Imaging Spectrometer mission (DESI) [38] mounted to the International Space Station (ISS), Italy’s Hyperspectral Precursor and Application Mission (PRISMA) [52], and the European Space Agency’s upcoming Copernicus Hyperspectral Imaging Mission for the Environment (CHIME) [53]. These developments open new avenues to employ deep learning and Self-Supervised Learning (SSL) for large-scale HSI analysis.



Figure 2. Mosaic of pseudo-RGB representatives from the SpectralEarth dataset to showcase a diverse range of landscapes including urban areas, agricultural land, deserts, forests, and water bodies. Each image is presented with a false-color composite using the first three principal components, highlighting the spectral diversity captured across environments.

Foundation models pre-trained with SSL demonstrated remarkable generalization capabilities with minimal fine-tuning in computer vision [51]. Subsequently, there has been a surge in developing geospatial foundation models, particularly for multispectral and high-resolution RGB imagery [64]. This line of research benefits from the abundance of publicly available satellite data from missions like Copernicus Sentinel-2 which provides petabytes of archive data for model training. In contrast, progress in foundation models for the hyperspectral domain has been hindered by the lack of large-scale HSI datasets for pre-training. Historically, access to hyperspectral imagery has been costly, with most benchmarks restricted to small-scale aerial imagery datasets [3]. While recent efforts [19, 55, 63] have begun to address this limitation, they still fall short in terms of data volume and geographic diversity to effectively train general hyperspectral foundation models.

To bridge this gap, we introduce *SpectralEarth*, a large-scale dataset derived from the EnMAP satellite mission, featuring over 538,974 hyperspectral image patches from 415,153 unique locations with global spatial distribution and cloud coverage below 10%. *SpectralEarth*, as illustrated in Figure 1, represents an important leap in scale, being significantly larger than existing HSI datasets, and spans a wide variety of landscapes to reflect the full diversity of spectral signatures. Compiled from 11,636 EnMAP scenes, the dataset volume exceeds 3TB in hyperspectral images. Notably, about 17% of its geospatial locations include timeseries data to enable multi-temporal HSI analysis. To effectively harness the rich information in hyperspectral data, we modify conventional vision backbones such as ResNet and ViT with a spectral adapter module. It enables such backbones to capture the unique spectral characteris-

tics of HSI. Using three popular SSL algorithms, MoCoV2 [15, 26], DINO [12] and MAE [27], we train these backbones on *SpectralEarth*, to provide a plurality of pretrained models for hyperspectral image analysis. To benchmark the efficacy of our models, we introduce four downstream datasets geospatially co-registered with EnMAP and DESIS imagery for land cover and crop type mapping. Our experiments demonstrate the potential of the foundation model paradigm to efficiently generalize across various hyperspectral imaging contexts, including adapting to data from alternative sensors with different spectral characteristics. Our contributions summarized:

- Assembly of *SpectralEarth*, a large-scale dataset comprising around 3.3TB of nearly cloud-free EnMAP hyperspectral images. *SpectralEarth* features a global geospatial distribution encompassing over 538,974 image patches from 415,153 unique geo-locations, 73,307 of which include multiple timestamps.
- Construction of four downstream datasets designed to benchmark classification and semantic segmentation tasks for HSI.
- Training of various foundation models on *SpectralEarth* to test and demonstrate their generalizability to multiple hyperspectral sensors. In addition, we demonstrate the models’ computational benefit through faster convergence in fine-tuning.

## 2. Related Work

### 2.1. Hyperspectral Datasets

Traditionally, hyperspectral benchmark datasets have been limited in geographical coverage, often confined to a single or a limited number of scenes [3, 30, 49, 60]. This limitation primarily roots in the expenses associated with air-

Dataset	# Img.	Size	Sensor	Bands	GSD	Multi-temporal
Indian Pines	1	145x145	AVIRIS	224	20m	×
KSC	1	512x614	AVIRIS	224	18m	×
Salinas	1	512x217	AVIRIS	224	3.7m	×
Pavia Uni.	1	610x340	ROSIS	103	1.3m	×
Pavia Center	1	1096x1096	ROSIS	102	1.3m	×
Botswana	1	1476x256	EO-1	242	30m	×
Cooke City	1	280x800	HyMap	126	3m	×
Houston Uni.	1	349x1905	ITRES-CASI	144	2.5m	×
SDFC	1	1201x201	HAHS	63	0.5m	×
Chikusei	1	2517x2335	Hyperspec-VNIR-C	128	2.5m	×
WHU-Hi	3	1217x303, 940x475, 550x400	Nano-Hyperspec	270-274	0.043-0.463m	×
Hyperview	~3k	avg. ~60x60	HySpex	150	2m	×
HySpecNet-11k	~11k	128x128	EnMAP	202	30m	×
MSST	~20k	64x64	EnMAP	200	30m	×
HSIHybrid	~4m	9x9	Multiple	Variable	Variable	×
HyperGlobal-450K	~447k	64x64	EO-1 and Gaoen-5B	242 and 330	30m	×
SpectralEarth	~538k	128x128	EnMAP	202	30m	✓

Table 1. *Summary of Hyperspectral Remote Sensing Datasets*: SpectralEarth contains close to nine gigapixels of 202 EnMAP bands each at 30m spatial resolution. This equates to an area of a little over six million square kilometers. The rows above the dashed line concern manually annotated datasets, while the part below lists unlabeled datasets for SSL.

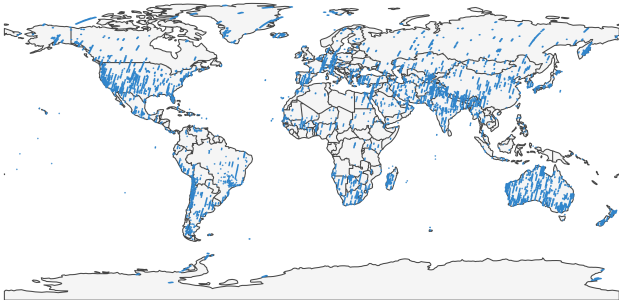


Figure 3. Geographical Distribution of SpectralEarth. The map depicts the global coverage of hyperspectral images within our dataset, demonstrating its extensive geographical scope.

borne hyperspectral sensor surveys on the one hand, and the collection of ground truth annotations and in-situ measurements on the other hand. While the collection of quality labels remains a challenge today, the increased accessibility to more cost-effective sensors, and the launch of hyperspectral satellite missions enabled coverage of larger geospatial regions by HSI. Developments in SSL and foundation models have also driven interest in creating large-scale unlabeled HSI datasets. For instance, the HySpecNet-11k [19] collected about 11,500 unlabeled hyperspectral patches from the EnMAP satellite. HySpecNet-11k is designed to benchmark (unsupervised) image compression techniques. Similarly, MSST [55] compiled a dataset of 19,792 EnMAP patches for SSL pre-training. While HySpecNet-11k and MSST have contributed to increase the scale of existing

HSI datasets, they remain limited in size to train foundation models. The recently introduced HyperGlobal-450K dataset [63] encompasses 450K HSI patches derived from 486 Hyperion EO-1 and 215 Gaoen-5B scenes. While this dataset significantly increases the scale of available HSI data, it presents the following limitations: First, its geographical distribution is less diverse, with a substantial part of the data concentrated in a few provinces of China. Moreover, it relies on imagery from the decommissioned EO-1 satellite. In contrast, SpectralEarth offers more extensive global coverage using data from the currently operational EnMAP satellite continuously collecting data. In addition, SpectralEarth is approximately five times larger in pixel count and it includes a temporal dimension increasing its value for pre-training of hyperspectral foundation models. A comparison of existing labeled and unlabeled HSI datasets provides Table 1.

## 2.2. Self-Supervised Learning for Remote Sensing

SSL emerged as a powerful paradigm for learning representations from unlabeled data [36]. Early SSL methods were based on engineered pretext tasks to encourage the model to learn distinct features by solving auxiliary problems such as image colorization [71], jigsaw puzzles [48], or rotation angle prediction [21]. Recently, progress in SSL has been primarily focused on two families of methods:

1. **Joint-Embedding Architectures:** These methods train models to generate consistent representations for augmented views of the same input, enforcing invariance to these augmentations. To avoid convergence to trivial

solutions, i.e., *model collapse* to a constant representation, several strategies have been developed: Contrastive approaches like MoCo [26] and SimCLR [14] use negative pairs to encourage learning discriminative representations. Clustering-based methods, such as SwAV [11], enforce balanced cluster assignment. Distillation-based frameworks like BYOL [22] and DINO [12] use an asymmetric teacher-student architecture. Methods like Barlow-Twins [70] and VICReg [6] explicitly use a loss regularization term to control the variance and feature correlation in the embedding space.

2. **Masked Image Modeling (MIM):** Inspired by masked language modeling, MIM methods predict missing parts of an image from a masked input. Existing methods differ in their reconstruction targets, loss functions, or network architectures. For example, Masked Autoencoder (MAE) [27] and SimMIM [68] reconstruct raw pixels, BEiT [5] predicts discrete visual tokens, while Data2Vec [4] and MSN [2] employ a teacher-student architecture to regress targets generated from the teacher branch.

In remote sensing, SSL techniques have been applied and adapted to multispectral and high-resolution RGB imagery. Manas et al. proposed SeCo [46], which compiled a 200K-location dataset comprising Sentinel 2 images with multiple temporal views (one per season) and introduced seasonal contrast augmentation. Their results supported the benefit of incorporating seasonal invariance in the training objective of contrastive methods. Building on this approach, Wang et al. proposed SSL4EO-S12 [65], which provided co-located Sentinel 2 and Sentinel 1 images and pre-trained models for both sensors. Subsequently, Stewart et al. extended this approach to Landsat imagery with SSL4EO-L [56], further expanding the available pre-training data, downstream datasets, and pre-trained models. Several studies have adapted MAE for remote sensing imagery. SatMAE [16] tokenized inputs across spectral and temporal dimensions, while Scale-MAE [54] introduced ground-sampled distance positional encoding for multi-scale imagery. GFM [47] assembled GeoPile, a pre-training dataset comprising high-resolution RGB images, by merging a variety of existing datasets. GeoPile was used to train an MAE model with an additional distillation loss guided by an ImageNet-22K pre-trained teacher. SpectralGPT [31] and S2MAE [42] proposed a hierarchical MAE pre-training approach based on a spatial-spectral vision transformer for Sentinel 2 imagery. CROMA [20] combined contrastive learning and MIM for SAR-Optical self-supervised learning. msGFM [23] proposed a multi-sensor MAE model with a cross-sensor reconstruction loss for paired images on RGB, Sentinel 1, Sentinel 2, and DSM data.

In the hyperspectral domain, most SSL works focus on

pixel-level classification (with or without spatial context) where the pre-training scene is the same as the test image [9, 10, 32, 33, 43, 44, 59]. While this approach is effective for classical HSI datasets, the learned representations cannot generalize across scenes. To address this issue, HSI-MAE [66] proposed HSIHybrid, a compilation of existing HSI datasets, and pre-trained an MAE-like model on it. While this approach effectively increases data diversity, it poses challenges when combining sensors with different characteristics, requiring pre-processing steps such as PCA to unify the number of spectral bands. Additionally, the scale of HSIHybrid remains limited for training HSI foundation models. Recent studies have explored collecting unlabeled HSI data for pre-training. For example, MSST [55] used MAE on EnMAP imagery, introducing decoupled spectral and spatial attention blocks to reduce the computational cost associated with spatial-spectral tokenization. HyperSIGMA [63] proposed an MAE-inspired approach with independent spectral and spatial transformers and evaluated their model on several hyperspectral downstream tasks. However, the data used for pre-training these models is less diverse than SpectralEarth. Additionally, these studies focus exclusively on ViTs and MAE, excluding ConvNets and other pre-training methodologies. In contrast, our work explores a more diverse set of architectures and pre-training strategies and provides a library of pre-trained models for HSI applications.

### 3. SpectralEarth & Benchmarks

This section introduces the SpectralEarth dataset and related downstream datasets for benchmarking. Additional details are provided in Appendix.

#### 3.1. SpectralEarth

**Data Acquisition.** The EnMAP data was sourced from the [DLR GeoPortal](#). A total of 11,636 tiles were retrieved via the portal’s graphical interface through a significant manual effort. All tiles were carefully selected based on human visual inspection. Cloud coverage was kept below ~10%. The selection process encompassed the entire EnMAP archive from April 2022 to April 2024. All acquired tiles underwent radiometric, geometric, and atmospheric corrections, resulting in Level-2A products.

**Data Pre-processing.** The EnMAP tiles have been split into geospatial patches—each of size 128x128 pixels where an individual pixel includes 224 bands. Bands dominated by water absorption were excluded due to the frequent presence of missing values (`no-data`). Removing those bands is a common practice in hyperspectral dataset creation [19, 60]. As a result, the total number of bands per image reduced to 202.

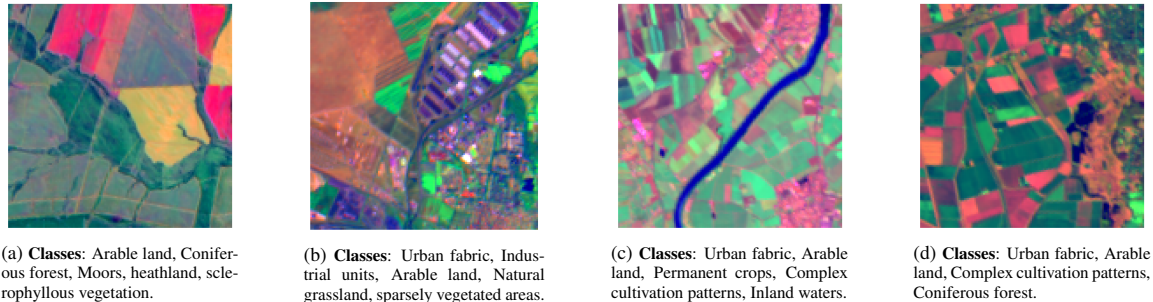


Figure 4. Sample pseudo-RGB images of the curated EnMAP-CORINE multi-label classification benchmark.

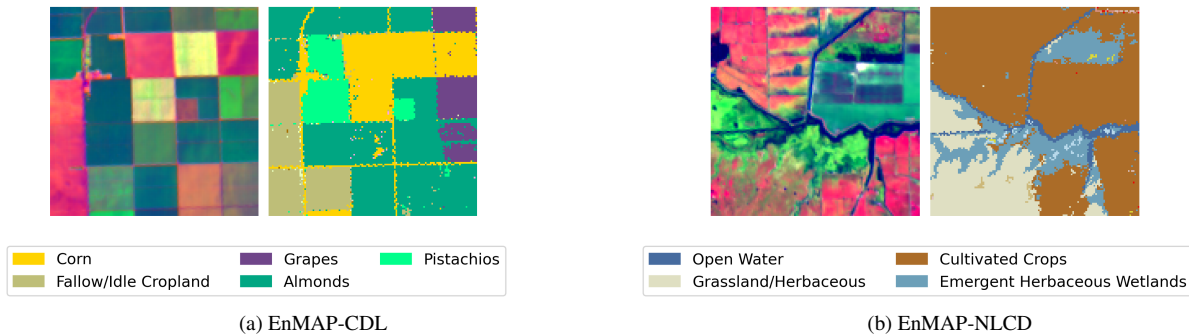


Figure 5. Sample image-mask (left-right) pairs of the curated EnMAP-CDL (a) and EnMAP-NLCD (b) semantic segmentation benchmarks.

**Temporal Views Extraction.** To exploit all available tiles, we utilized overlaps between EnMAP data acquisitions to generate time series of EnMAP patches<sup>1</sup>. At the same time SpectralEarth data patches for a fixed geo-location never overlap. This process required (a) identification of tiles that overlap spatially to (b) extract patches from the intersection of those tiles. Time series include valuable information on landscape evolution and provide characteristic signals for seasonal variation—an asset for contrastive learning [46, 65]. Algorithm 1 outlines the steps taken to generate temporal positives by high-level pseudo-code.

As a result of Algorithm 1 we identified a few long time series in the EnMAP archive. Those involving more than 25 intersecting tiles. Calculating intersections of all subsets was computationally intractable due to combinatorial explosion. To address this, we implemented several heuristics to optimize the computation:

1. Consider only a subset of possible intersections using a breadth-first search (BFS) approach.
2. Avoid redundant computations across tiles.
3. Parallelization of the code across all connected components of the overlap graph.

Following this approach, we extracted 73,307 non-overlapping locations with multiple timestamps. For areas

<sup>1</sup>EnMAP records hyperspectral imagery based on a schedule generated from user requests [37], i.e. the identification of spatially aligned patches for multiple timestamps is a valuable asset our data curation provides.

with a single timestamp we patchified avoiding any spatial overlap. Correspondingly, in SpectralEarth we extracted 415,153 locations with a spatial extent of 128x128 pixels, totaling 538,974 patches. Figure 6 illustrates the distribution of timestamp counts in SpectralEarth. Over the two-year’s period, 17.5% of locations were covered by more than one timestamp in the EnMAP archive—with the majority having only two timestamps. This highlights the challenge of collecting extensive hyperspectral time series data with broad geographical coverage today. Missions such as ESA’s CHIME satellite constellation [53] will eventually resolve the issue.

The spatial coverage of SpectralEarth showcases the dataset’s global diversity, cf. Figure 3. Notably, the data distribution varies across geo-locations. EnMAP is a mission with scheduled acquisition depending on areas of interest.

### 3.2. Downstream Tasks

To evaluate the models pretrained on SpectralEarth, we assembled four downstream datasets for benchmarking. Each benchmark involves a subset of EnMAP or DESIS images, aligned with specific geospatial products with focus on specific aspects of land cover and agricultural analysis. While the labels in these datasets carry some inherent uncertainty, they are sufficiently accurate for a proof-of-concept evaluation of model performance. Similar strategies have previously been employed to create remote sens-

---

**Algorithm 1** Temporal Views Extraction

---

```
1: procedure MAIN PROCEDURE
2:    $tiles \leftarrow \text{EnMAPData}$ 
3:    $overlap\_graph \leftarrow \text{GETOVERLAPS}(tiles)$ 
4:    $R\_tree \leftarrow K_0 \triangleright$  empty tree, for SpectralEarth patches
5:   for  $tile$  in  $tiles$  do
6:      $combinations$ 
7:      $\leftarrow \text{BUILDCOMBINATIONS}(tile, overlap\_graph)$ 
8:     for  $tile\_subset$  in  $combinations$  do
9:        $intersection \leftarrow \text{INTERSECTION}(tile\_subset)$ 
10:       $patches \leftarrow \text{PATCHIFY}(intersection)$ 
11:       $\text{UPDATE}(R\_tree, patches)$ 
12:    end for
13:  end for
14: end procedure

15: function BUILDCOMBINATIONS( $tile, overlap\_graph$ )
16:   $combinations \leftarrow \text{GETEDGES}(tile, overlap\_graph)^2$ 
17:  for subset size  $n$  in  $[3, 4, \dots]$  do
18:    get  $n$ -tuples from  $(n-1)$ -tuples in  $combinations$ 
19:    compute intersections of all  $n$ -tuples
20:    keep largest  $n$ -tuples by area
21:    if no valid  $n$ -tuple found then
22:      break
23:    end if
24:    add  $n$ -tuples to  $combinations$ 
25:  end for
26:  return  $combinations$ 
27: end function
```

---

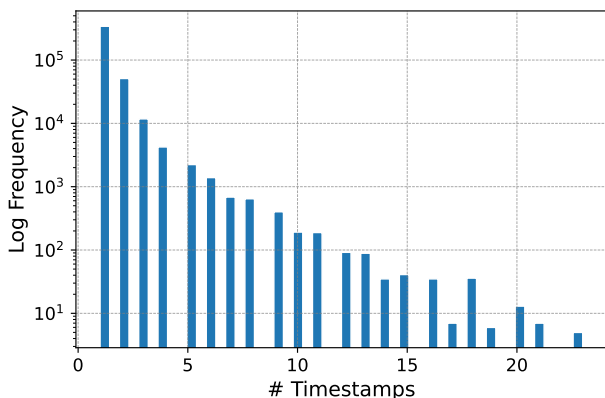


Figure 6. Histogram representing the number of timestamps (log-scale) for geo-locations covered by SpectralEarth. The majority of locations include one timestamp, while the remaining ones mostly consist of pairs and triplets.

ing datasets [34, 56, 57].

**EnMAP-CORINE: Land Cover Classification.** This dataset pairs EnMAP imagery with the [CORINE land cover database](#) for Europe. The CORINE land cover map has

a 100m spatial resolution, which is coarse-grained relative to EnMAP’s 30m resolution. Our SpectralEarth image patches correspond to approximately 38x38 CORINE land cover pixels. Consequently, we create a multi-label classification benchmark where each SpectralEarth patch is annotated with the set of CORINE classes covered. The resulting subset, called EnMAP-CORINE, includes 11,000 patches, each multi-labeled with 19 distinct classes. These classes have been aggregated from the 44 categories defined in CORINE following the taxonomy proposed by BigEarthNet-MM [58]. Example patches from four diverse scenes are depicted in Figure 4.

**EnMAP-CDL: Crop Type Segmentation.** This dataset aligns EnMAP images with the Cropland Data Layer (CDL) [8] product for the United States. The CDL map is published annually by the [USDA](#)’s National Agricultural Statistics Service since 2008. It targets agricultural crop classification. In addition to classes for cultivated land such as Soybeans and Winter Wheat, CDL encompasses non-cultivated areas like Grassland and Shrubland. To minimize the impact of seasonal variations on crop classification, the dataset utilizes SpectralEarth patches from the summers of 2022 and 2023. Given the strong imbalance among CDL classes, we resampled the class distribution to set up a more balanced representation. The resulting dataset comprises 2,000 patches with a total of 20 classes.

**EnMAP-NLCD: Land Cover Segmentation.** This downstream dataset leverages the National Land Cover Database (NLCD) [17] from the U.S. Geological Survey (USGS) to provide pixel-level land cover annotations. The NLCD map, a comprehensive land cover product, has been published every 2–3 years since 2001, with data available back to 2019. The resulting dataset contains 15,000 patches, each annotated with pixel-wise land cover class labels from one out of the 15 land cover classes.

**DESI-CDL: Crop Type Segmentation.** The DESI-CDL dataset contains images captured for the summers of 2021, 2022 and 2023 from the DESI (DLR Earth Sensing Imaging Spectrometer Mission) instrument, matched with the corresponding CDL mask for crop segmentation. DESI images are generated at 30m spatial resolution with 235 bands covering wavelengths from 400 nanometers through a micron. The resulting dataset comprises 1,000 images with 19 classes.

## 4. Hyperspectral Foundation Models

This section presents the design choices behind our models, including the choice of SSL algorithms and network architecture.

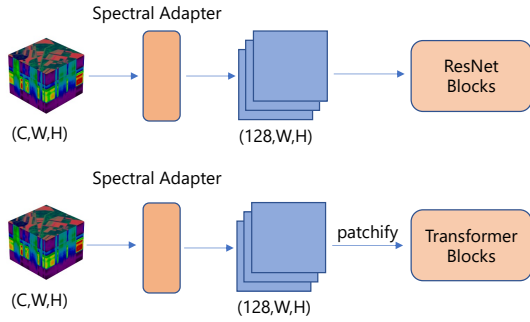


Figure 7. Schematic representation of the proposed backbones tailored for HSI. We augment classical ResNet and ViT with a spectral adapter to process spectral information effectively.

#### 4.1. Pre-training Algorithms

Hyperspectral data has very different characteristics compared to natural images. Therefore, traditional SSL leaderboards in computer vision may not directly translate to the hyperspectral domain. To address this gap, we explore a broad range of SSL methods to establish a set of baseline pretrained models for hyperspectral imagery. We use MoCo-V2 [26] and DINO [12] for their effectiveness in frozen encoder performance [51] and their compatibility with both CNNs and ViTs. Furthermore, we include MAE [27] for its strong performance in fine-tuning scenarios. Together, these methods form a representative set of algorithms to investigate SSL in the hyperspectral domain.

#### 4.2. Network Architectures

Since we aim for large-scale coverage and pre-training with spaceborne imagery, our models must operate on large patches instead of pixels or small patches, as traditionally done in the hyperspectral literature. Most models developed at the pixel level in HSI literature do not scale well with large patches [28, 29, 72]. On the other hand, models like ResNet [24] and ViT [18] are designed to handle larger spatial contexts. Therefore, we seek to adapt these architectures for hyperspectral imaging. A key challenge is that classical ResNet and ViTs treat spectral bands independently, failing to capture the correlations between adjacent bands and the overall characteristics of the spectrum. Our models should address the following requirements for hyperspectral imaging:

- **Spectral Feature Extraction:** We aim to extract features from both the spatial and the spectral domain.
- **Adaptability to Diverse Sensors:** The architecture should accommodate variability in the number of spectral bands. This property is important when transferring pretrained models to different sensors.
- **Preserving Fine-Grained Details:** Natural images often

deal with large objects compared to medium-resolution remote sensing data. Therefore, the spatial downscaling in classical vision models can lead to a significant loss of details. Our architecture needs to preserve this fine-grained information.

- **Computational Efficiency:** 3D convolution or tokenizing the image in the spectral dimension is computationally expensive for large models. We seek for adaptation of classical architectures with minimal overhead.

To meet these requirements, we follow a pragmatic approach and implement a simple modular design, integrating 1D convolutional layers as a Spectral Adapter at the onset of the standard vision backbones, as depicted in Figure 7. These layers perform convolutions across the spectral dimension, generating feature maps for the core backbone. Specifically:

- *Spectral ResNet:* We replace the stem layers with three 1D convolutional layers and pooling, allowing the network to process spectral information effectively before the residual backbone. By removing the original stem layers in the ResNet architecture, we avoid the 4x downscaling factor of the image to better capture fine-grained details.
- *Spectral ViT:* The 1D convolutions and pooling are placed before the patch embedding layer, ensuring that the transformer receives fixed-size spectral features as input. We use 4x4 patches instead of the typical 16x16 patches, which helps maintain fine spatial details and better preserves spectral information at the patch projection layer.

This simple strategy results in an architecture that can be used on various hyperspectral sensors while leveraging a lightweight adapter for spectral feature extraction. Similar designs have been used effectively for spectral-spatial classifiers in the HSI literature [1]. Our approach extends this idea to foundation models, enabling the extraction of both spatial and spectral features while avoiding the extra computational cost incurred by 3D convolutions or spatial-spectral tokenization in ViTs.

## 5. Experimental Setup

### 5.1. Self-Supervised Pre-training

We pre-train a spectral ResNet-50 (Spec. RN50) and a spectral ViT-S (Spec. ViT-S) with MoCo-V2, DINO, and MAE. For larger models, Spec. ViT-Base(B)/Large(L)/Huge(H)/Giant(g), we restrict the experiments to MAE given the high computational cost. For ViT-g, we follow the implementation from [51]. We use the augmentations from SimCLR [14] without color-jittering and gray-scale for DINO and MoCo-V2 to avoid distorting spectral information. When available, we use the

temporal views as positive pairs for MoCo-V2 and DINO. For MAE, we mask 90% of the tokens. We pretrain over 100 epochs for MoCo-V2 and DINO, and 200 epochs for MAE with a batch size of 256 images. We use a `StepLR` scheduler for MoCo-V2, and `CosineAnnealingLR` for DINO and MAE.

## 5.2. Downstream Tasks

**Multi-label classification on EnMAP-CORINE.** We append a linear layer to the pretrained encoders and train the models with Binary Cross-Entropy loss for 100 epochs.

**Semantic segmentation on EnMAP-CDL/-NLCD and DESIS-CDL.** We use a lightweight transfer protocol for the segmentation tasks, following previous works [22, 26]. We train for 100 epochs with a cross-entropy loss. The pretrained encoders are converted into segmentation models as follows:

- **ResNet:** We remove all strides from convolutions, replace them with atrous convolutions, and append two final convolutional layers.
- **ViT:** We reshape the tokens from the last layer and add two additional convolutional layers with upscaling to recover the full spatial resolution.

**Parameter regression on Hyperview.** We use the training set of the Hyperview challenge [49] to evaluate cross-sensor transferability. Hyperview is a soil parameter estimation dataset comprising 1,732 hyperspectral patches with 150 spectral bands. Each patch is annotated with four soil parameters, including potassium ( $K$ ), phosphorus pentoxide ( $P_2O_5$ ), magnesium ( $Mg$ ), and acidity  $pH$ . For this downstream task, we append two fully connected layers to the backbones. The models are optimized based on the normalized MSE criterion defined in Section 5.4 with the AdamW optimizer for 200 epochs.

## 5.3. Evaluation Protocols

We consider multiple evaluation protocols with various levels of fine-tuning of the pretrained models.

- **Frozen Encoder:** Evaluates the quality of learned representations without fine-tuning the backbone. It is the most common evaluation protocol in the SSL literature [7, 51].
- **Fine-tuning:** Fine-tuning of all model parameters on downstream datasets to evaluate the transferability of the pretrained weights.
- **Fine-tuning Adapter:** While frozen encoder evaluation is a common measure of the quality of learned representations, it does not yield optimal results. In remote sensing, it is often beneficial to adapt the model to the specific distribution of the downstream dataset, which can be influenced by several factors: geo-location, atmospheric

conditions, seasonal changes, etc. Additionally, the relevance of individual spectral bands may vary depending on the downstream task. Therefore, we consider an intermediate setting where only the initial spectral adapter block is fine-tuned.

## 5.4. Evaluation Metrics

Depending on the nature of the downstream task, we report the following metrics:

- **Classification:** The multi-label F1-score is reported for the EnMAP-CORINE dataset.
- **Segmentation:** The mean Intersection over Union (mIoU) is reported for the EnMAP-CDL, EnMAP-NLCD and DESIS-CDL datasets.
- **Regression:** For the Hyperview dataset, we follow the metric defined in the challenge [49]: let  $MSE_i, i \in [1, 4]$  be the mean squared error of the predictor for soil parameter  $i$ . Let  $MSE_i^{base}$  be the corresponding MSE of a base predictor returning the mean value of the soil parameter, calculated over the training set. The reported normalized MSE is defined as:  $MSE_{norm} = \sum_{i=1}^4 MSE_i / MSE_i^{base}$ .

## 6. Benchmark Results

Our main results are summarized in Tables 2 and 3. We include random initialization baselines for each downstream task, along with our pretrained models. Due to hundreds of spectral channels of the SpectralEarth patches, a comparison with RGB-ImageNet weights or multispectral pretrained models is of little use.

### 6.1. Comparing SSL Algorithms

Table 2 summarizes our results for three SSL algorithms with the Spec. RN50 and Spec. ViT-S backbones.

**EnMAP-CORINE.** Pretrained models outperform random weights in linear evaluation for MoCo-V2 and DINO, with DINO yielding the best results, demonstrating the ability of joint-embedding methods to learn robust representations, even in the absence of fine-tuning. Additionally, we observe that MAE under-performs in linear probing, which is consistent with existing literature [41]. This can be attributed to the reconstruction pre-training objective, which focuses on low-level features, whereas joint-embedding methods learn more global and semantic representations. For full fine-tuning, pretrained models are on par with/slightly outperform training from scratch.

Fine-tuning the adapter yields a notable performance boost compared to linear evaluation. This significant performance improvement aligns with reports in the literature [40]: fine-tuning early network layers is an efficient compromise between frozen weights vs. complete fine-tuning. In terms of F1-score, only fine-tuning the adapter

Evaluation protocol (# of trainable params.)	Init Weights	EnMAP-CORINE (F1 Score)		EnMAP-CDL (mIoU)		EnMAP-NLCD (mIoU)	
		Spec. RN50	Spec. ViT-S	Spec. RN50	Spec. ViT-S	Spec. RN50	Spec. ViT-S
Frozen Encoder (0)	Random	70.53	70.42	44.72	46.52	35.86	36.85
	MoCo-V2	73.97	73.60	<b>51.66</b>	50.37	<b>41.98</b>	39.85
	DINO	<b>76.64</b>	<b>75.06</b>	51.53	51.01	41.77	40.31
	MAE	–	72.72	–	<b>51.37</b>	–	<b>41.17</b>
Full Fine-tuning (>20M)	Random	78.31	77.78	57.53	55.07	<b>48.18</b>	45.95
	MoCo-V2	<b>78.57</b>	78.40	<b>58.10</b>	55.84	48.09	45.78
	DINO	77.98	78.34	57.77	55.70	47.75	45.71
	MAE	–	<b>78.66</b>	–	<b>57.66</b>	–	<b>47.82</b>
Fine-tune Adapter (56K)	MoCo-V2	76.27	76.12	<b>55.36</b>	54.37	<b>44.66</b>	43.40
	DINO	<b>78.43</b>	<b>77.95</b>	55.26	53.50	44.41	43.00
	MAE	–	76.80	–	<b>54.61</b>	–	<b>43.92</b>

Table 2. Benchmark results of the SpectralEarth downstream tasks for Spec. RN50 and Spec. ViT-S under different evaluation protocols: frozen backbone, full fine-tuning, and fine-tuning the spectral adapter only. We report the number of trainable parameters in the pretrained backbones, excluding task-specific heads. The best scores of each evaluation protocol-backbone are in **bold**.

Evaluation Protocol	EnMAP-CORINE (F1 Score)				EnMAP-CDL (mIoU)				EnMAP-NLCD (mIoU)			
	B	L	H	g	B	L	H	g	B	L	H	g
Training from Scratch	76.99	77.24	<b>77.28</b>	76.85	54.79	54.50	<b>54.83</b>	54.74	<b>45.96</b>	45.62	45.53	45.58
Frozen Encoder	74.72	75.07	<b>76.06</b>	75.33	51.20	53.14	<b>53.19</b>	52.77	40.52	42.88	<b>43.32</b>	42.63
Full Fine-tuning	79.05	79.18	<b>79.80</b>	78.38	57.70	<b>58.19</b>	58.06	57.86	48.10	<b>48.37</b>	48.28	48.08
Fine-tune Adapter	77.09	77.79	<b>77.94</b>	77.86	54.79	<b>55.35</b>	55.14	54.90	43.97	44.46	44.67	<b>44.73</b>

Table 3. Benchmark results for large vision transformers with varying sizes pre-trained on SpectralEarth with MAE. Models are evaluated under three protocols: frozen encoder, full fine-tuning, and fine-tuned adapter. Training from scratch is reported as a baseline. The best score for each protocol is highlighted in **bold**.

(0.3% of network parameters) with DINO matches training from scratch, highlighting the efficient adaptability of our pretrained models.

**EnMAP-CDL.** SSL pre-training yields improved results over random initialization, with MoCo overall performing best for Spec. RN-50, while MAE performs best for Spec. ViT-S with full fine-tuning. Moreover, fine-tuning the adapter enables the spectral convolutions to adjust to the distribution of the downstream dataset, effectively bridging the performance gap between linear evaluation and full fine-tuning. For the Spec. ViT-S, fine-tuning the spectral adapter is only half a point lower than training from scratch. As a general observation, Spec. RN50 slightly outperforms Spec. ViT-S on EnMAP-CDL for all evaluation protocols. This shows that, despite the rise of vision transformers, convolutional networks remain highly effective in remote sensing, especially with smaller datasets.

**EnMAP-NLCD.** On the NLCD downstream task, the frozen pretrained backbones yield improvements over random weights but remain significantly worse than training from scratch. Notably, MAE outperforms training from scratch by 2% of mIoU, demonstrating its strong transferability with fine-tuning. Conversely, training from scratch shows competitive performance, matching full fine-tuning for MoCo-V2 and DINO. This observation is aligned with findings from previous studies [25, 26] suggesting that training from scratch is a strong baseline. A discussion on the influence of the number of fine-tuning epochs is provided in Section 6.5.

## 6.2. Scaling-up Pretrained Models

Recent studies have shown significant performance gains through model scaling in SSL [27, 51]. Consequently, recent geospatial foundation models are exploring ViT architectures with hundreds of millions of parameters [31, 34,

63]. We investigate model scaling on SpectralEarth by pre-training Spec. ViT architectures of varying sizes: Base (B), Large (L), Huge (H), and Giant (g). Our findings are presented in Table 3. We observe that MAE consistently outperforms training from scratch across all model sizes. Remarkably, fine-tuning the adapter, which corresponds to 56K trainable parameters, matches or surpasses training from scratch for the EnMAP-CORINE and EnMAP-CDL tasks. Moreover, we observe initial benefits from scaling up the models up to Spec. ViT-L/H. However, additional increases in model size do not improve performance, possibly due to the size of the pretraining dataset. While SpectralEarth is significantly larger than previous HSI datasets, it remains smaller than the datasets used in computer vision for training state-of-the-art models [51]. This highlights the importance of scaling the data when training large vision transformers in remote sensing.

### 6.3. Efficient Fine-tuning

**Model convergence.** Using a pretrained model can speed up convergence during fine-tuning, hence reducing the computational cost of training deep neural networks. To assess this for our models, we compare the training efficiency of Spec. RN50 models pretrained with DINO relative to training from scratch on the CORINE and CDL benchmarks. Figure 8 displays the evolution of the validation metrics across training epochs. We observe that pretrained models converge more rapidly, particularly in the early stages of training. Notably, fine-tuning matches the 100 epochs performance of training from scratch in  $\sim 30$  epochs for EnMAP-CDL. These results highlight the computational advantage of using our pretrained models compared to training from scratch.

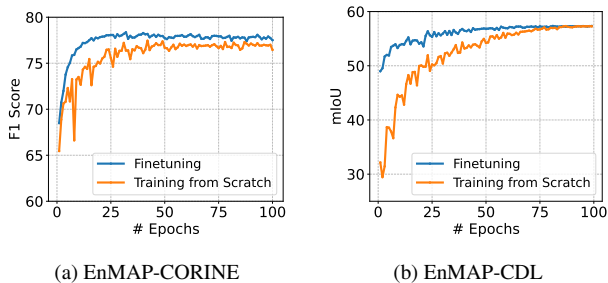


Figure 8. Comparison of convergence speed for fine-tuning and training from scratch on EnMAP-CORINE and EnMAP-CDL for a Spec. RN50 backbone.

**Parameter-efficient fine-tuning.** Foundation models are typically evaluated in linear probing to assess the quality of the learnt representations [26]. While a frozen encoder can achieve competitive performance, fine-tuning often surpasses it—at a higher computational cost. We experiment

with the progressive unfreezing of network layers as a compromise between both scenarios. As depicted in Figure 9, fine-tuning the first two blocks of a pretrained Spec. RN50 produces results that closely resemble full fine-tuning. This demonstrates the cost- and energy efficiency of our pre-trained models for downstream tasks.

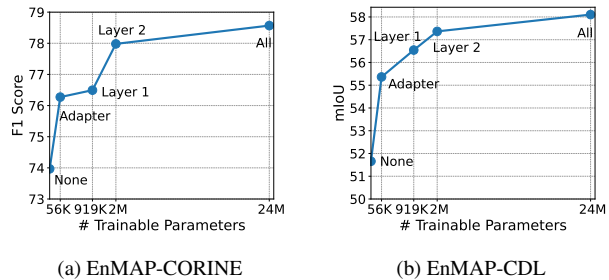


Figure 9. Impact of incremental parameter unfreezing on EnMAP-CORINE and EnMAP-CDL with a pre-trained Spec. RN50 model.

**Training with limited labels.** Pre-trained models are very useful when labeled data is scarce [50]. To assess this, we evaluate the performance of the Spec. ViT-L model, pre-trained with MAE, on varying subset sizes of EnMAP-CORINE and EnMAP-NLCD datasets. The results, reported in Figure 10, demonstrate the benefits of pre-training across all data regimes. In particular, we observe large gaps of 9 points in F1 score for EnMAP-CORINE, and 5 points in mIoU for EnMAP-NLCD, when using 5% of the labels compared to training from scratch. Interestingly, in lower data regime scenarios, fine-tuning the adapter only suffices to outperform training from scratch. This demonstrates the generalizability of the features learned from pre-training.

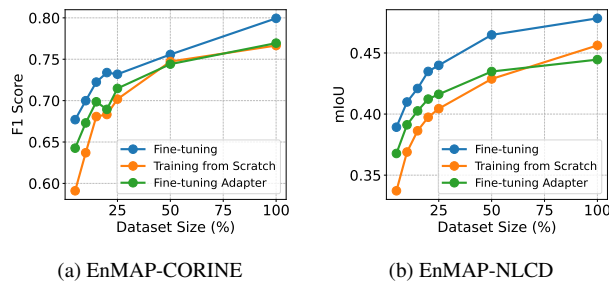


Figure 10. Impact of the size of the downstream dataset evaluated on EnMAP-CORINE and EnMAP-NLCD for the Spec. ViT-L model.

### 6.4. Cross-Sensor Transferability

To assess the transferability of our pretrained models to other sensors, we evaluate them on the Hyperview and DESIS-CDL datasets. Images in both datasets have been

collected by sensors with different spectral characteristics from EnMAP. In Table 4, we evaluate the Spec. RN-50 architecture across different fine-tuning protocols. We observe consistent improvements over training from scratch when using a pretrained model for both datasets. Unsurprisingly, the frozen encoders perform relatively poorly due to the difference in the sensor. However, fine-tuning the spectral adapter is sufficient to close most of the performance gap with fine-tuning. Notably, fine-tuning the adapter only outperforms training from scratch on Hyperview, which can be attributed to overfitting on this dataset.

Evaluation Protocol	Hyperview	DESIS-CDL
	Normalized MSE (%) ↓	mIoU (%) ↑
Random Frozen Encoder	96.29	48.60
Training from Scratch	92.09	59.85
Frozen Encoder	92.43	51.85
Fine-tune Adapter	<b>90.08</b>	58.03
Full Fine-tuning	92.68	<b>60.55</b>

Table 4. Comparison of SSL versus training from scratch on Hyperview and DESIS-CDL with Spec. RN50 backbone. We use DINO for Hyperview and MoCo-V2 for DESIS-CDL.

### 6.5. Ablation Studies

**Impact of temporal positives.** Temporal positives provide a natural data augmentation for joint-embedding methods and have demonstrated their benefits for multi-spectral imagery [46, 56, 65]. Given that only a subset of SpectralEarth includes temporal positives, it is unclear whether using temporal pairs significantly contributes to the overall performance of the pretrained models. To analyze their effect, we pretrain a Spec. RN50 using DINO with and without temporal pairs. Results in Table 5 confirm that excluding temporal positives degrades performance, with the effect most pronounced in frozen encoder evaluation.

Table 5. Impact of temporal positives. All models are pre-trained on SpectralEarth with MoCo-V2. We report F1 Score for EnMAP-CORINE and mIoU for EnMAP-CDL.

Model	EnMAP-CORINE (F1)		EnMAP-CDL (mIoU)	
	Frozen	Fine-tune	Frozen	Fine-tune
w/ TP	<b>76.64</b>	<b>77.98</b>	<b>51.53</b>	<b>57.77</b>
w/o TP	74.85	75.36	49.93	57.48

**How much data is needed for pre-training?** To answer this question, we explore the impact of dataset size by pre-training a Spec. RN50 with DINO on randomly sampled subsets of SpectralEarth with sizes 10K, 25K, 50K, 100K,

and 200K locations. We conduct frozen-encoder evaluation on EnMAP-CORINE and EnMAP-CDL. Figure 11 summarizes our findings. We observe a consistent improvement in performance metrics as the scale of the pre-training dataset increases from 10k samples to the full size of SpectralEarth. While the performance on EnMAP-CDL appears to saturate, the F1 Score for EnMAP-CORINE still increases, despite the small size of Spec. RN50. This trend confirms the importance of large-scale datasets for pre-training hyperspectral foundation models.

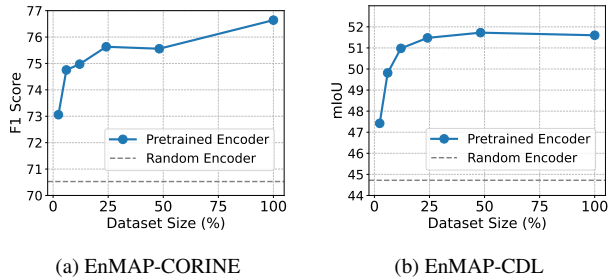


Figure 11. Frozen encoder evaluation of Spec. RN50 on EnMAP-CORINE and EnMAP-CDL tasks with varying pre-training dataset sizes.

**Importance of the patch size.** Medium-resolution remote sensing imagery requires more fine-grained detail preservation than natural imagery, especially for segmentation tasks. This aspect is sometimes overlooked in the literature, where vision transformers with a patch size of 16x16 or 8x8 are commonly used as backbones to pre-train foundation models to reduce the computational cost [16, 34, 63, 69]. We argue that a smaller image size with a smaller patch size can lead better trade-offs, particularly for HSI imagery where pixel information is rich and should not be heavily compressed in the embedding space. To analyze the impact of the patch size, we pre-trained Spec. ViT-S using MAE with patch sizes of 4x4, 8x8 and 16x16. Results in Figure 12 show that smaller patches consistently improve performance for segmentation tasks. This is further supported by qualitative results in Figure 13, where models with smaller patches produce more refined segmentation maps. These results are consistent with the performance gap between ViT-based foundation models and ConvNet baselines observed in previous studies [67]. In practice, using additional trainable parameters to extract high-resolution features in combination with a pre-trained ViT can mitigate this issue.

**Masking ratio in MAE.** Given our small 4x4 patch size for Spec. ViT models, we expect a higher masking ratio is needed for MAE compared to the usual 75% used in Com-

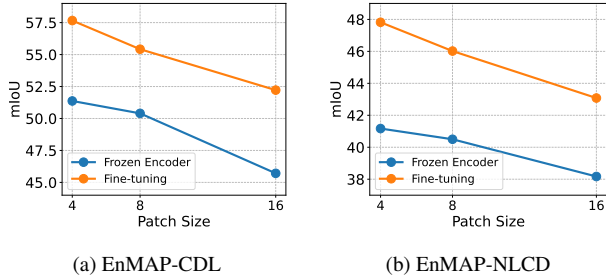


Figure 12. Impact of the patch size for a pre-trained Spec. ViT-S evaluated on the EnMAP-CDL and EnMAP-NLCD datasets.

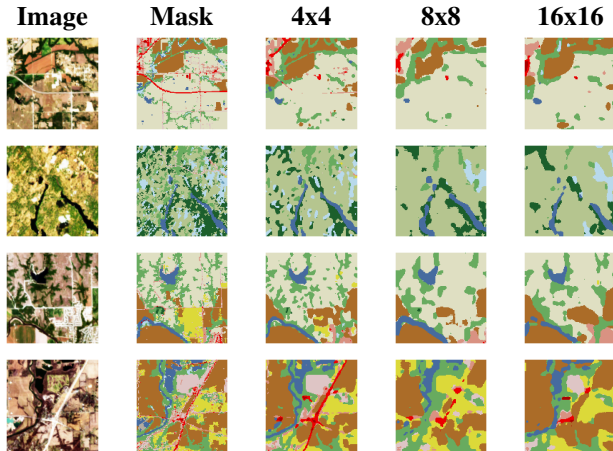


Figure 13. Impact of the patch size in the Spec. ViT-S model on EnMAP-NLCD. From left to right respectively: RGB visualization of the input image, ground truth (GT) mask, and predictions with 4x4, 8x8, and 16x16 patch sizes.

puter Vision [27]. To confirm this hypothesis, we pre-train Spec. ViT-S using MAE with different masking ratios, from 75% to 99%. Given MAE’s poor linear probing results for the classification task, we focus on the segmentation downstream tasks. Results in Figure 14 show that we obtain good representations even with an aggressive 95% masking, which enables faster pre-training as fewer tokens need to go through the encoder.

Table 6. Impact of the spectral adapter in the Spec. RN50 architecture. All models are pre-trained on SpectralEarth with MoCo-V2.

Model	EnMAP-CORINE (F1)		EnMAP-CDL (mIoU)	
	Frozen	Fine-tune	Frozen	Fine-tune
w/o Adapter	72.82	77.10	47.85	55.43
w/ Adapter	<b>73.97</b>	<b>78.57</b>	<b>51.66</b>	<b>58.10</b>

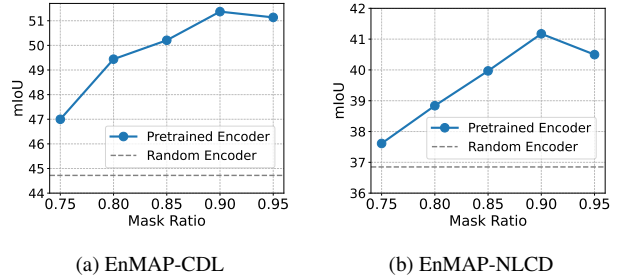


Figure 14. Impact of the masking ratio in MAE evaluated on EnMAP-CDL and EnMAP-NLCD for the Spec. ViT-S model.

**Impact of the spectral adapter.** To assess the impact of the spectral adapter, we compare the classical ResNet-50 with our modified architecture, Spec. RN50. We adjust the first convolutional layer of the ResNet-50 model to accommodate the 202 input bands. Both models are pre-trained with MoCo-V2 and evaluated on the EnMAP-CORINE and EnMAP-CDL datasets. The results are summarized in Table 6. Spec. RN50 consistently outperforms the standard ResNet-50 in both frozen encoder evaluation and full fine-tuning. This result confirms the importance of a dedicated spectral feature extractor when dealing with hyperspectral images, particularly for tasks requiring fine-grained spectral discrimination.

## 7. Conclusion

We introduce SpectralEarth, a large-scale dataset derived from EnMAP imagery as basis for SSL methodologies in the hyperspectral domain. We leveraged SpectralEarth to pre-train foundation models based on popular SSL algorithms. Extensive evaluation on several downstream tasks benchmarked the pre-trained models. Our results demonstrate the effectiveness of models pre-trained on SpectralEarth to improve performance and to reduce computational costs for downstream applications. We believe that the insights derived from this study serve as a basis for future development in SSL for hyperspectral imagery.

As it stands, we encourage further effort to construct additional hyperspectral benchmark datasets. Covering tasks such as unmixing enables a more comprehensive assessment in terms of generalizability of hyperspectral foundation models. In particular, transferability across different hyperspectral sensors remains a challenging problem. Moreover, exploration of a wider range of architectures and SSL algorithms, beyond the Spectral ResNet-50 and ViT models employed in this work, may provide a more comprehensive toolbox for practical deep learning on HSI. Last but not least, exploration and benchmarking multi-sensor SSL methods entails a promising endeavor toward more general geospatial foundation models.

## References

- [1] Muhammad Ahmad, Salvatore Distifano, Manuel Mazzara, and Adil Mehmood Khan. Traditional to transformers: A survey on current trends and future prospects for hyperspectral image classification. *arXiv preprint arXiv:2404.14955*, 2024. 7
- [2] Mahmoud Assran, Mathilde Caron, Ishan Misra, Piotr Bojanowski, Florian Bordes, Pascal Vincent, Armand Joulin, Mike Rabbat, and Nicolas Ballas. Masked siamese networks for label-efficient learning. In *European Conference on Computer Vision*, pages 456–473. Springer, 2022. 4
- [3] Nicolas Audebert, Bertrand Le Saux, and Sébastien Lefèvre. Deep learning for classification of hyperspectral data: A comparative review. *IEEE geoscience and remote sensing magazine*, 7(2):159–173, 2019. 2
- [4] Alexei Baevski, Wei-Ning Hsu, Qiantong Xu, Arun Babu, Jiatao Gu, and Michael Auli. Data2vec: A general framework for self-supervised learning in speech, vision and language. In *International Conference on Machine Learning*, pages 1298–1312. PMLR, 2022. 4
- [5] Hangbo Bao, Li Dong, Songhao Piao, and Furu Wei. Beit: Bert pre-training of image transformers. In *International Conference on Learning Representations*, 2021. 4
- [6] Adrien Bardes, Jean Ponce, and Yann Lecun. Vicreg: Variance-invariance-covariance regularization for self-supervised learning. In *ICLR 2022-International Conference on Learning Representations*, 2022. 4
- [7] Adrien Bardes, Jean Ponce, and Yann LeCun. Vicregl: Self-supervised learning of local visual features. *Advances in Neural Information Processing Systems*, 35: 8799–8810, 2022. 8
- [8] Claire Boryan, Zhengwei Yang, Rick Mueller, and Mike Craig. Monitoring us agriculture: the us department of agriculture, national agricultural statistics service, cropland data layer program. *Geocarto International*, 26(5):341–358, 2011. 6
- [9] Nassim Ait Ali Braham, Julien Mairal, Jocelyn Chanussot, Lichao Mou, and Xiao Xiang Zhu. Enhancing contrastive learning with positive pair mining for few-shot hyperspectral image classification. *IEEE Journal of Selected Topics in Applied Earth Observations and Remote Sensing*, 2024. 4
- [10] Xianghai Cao, Haifeng Lin, Shuaixu Guo, Tao Xiong, and Licheng Jiao. Transformer-based masked autoencoder with contrastive loss for hyperspectral image classification. *IEEE Transactions on Geoscience and Remote Sensing*, 2023. 4
- [11] Mathilde Caron, Ishan Misra, Julien Mairal, Priya Goyal, Piotr Bojanowski, and Armand Joulin. Un-supervised learning of visual features by contrasting cluster assignments. *Advances in neural information processing systems*, 33:9912–9924, 2020. 4
- [12] Mathilde Caron, Hugo Touvron, Ishan Misra, Hervé Jégou, Julien Mairal, Piotr Bojanowski, and Armand Joulin. Emerging properties in self-supervised vision transformers. In *Proceedings of the IEEE/CVF international conference on computer vision*, pages 9650–9660, 2021. 2, 4, 7
- [13] S Chabrilat, E Ben-Dor, J Cierniewski, Cécile Gomez, T Schmid, and Bas van Wesemael. Imaging spectroscopy for soil mapping and monitoring. *Surveys in Geophysics*, 40:361–399, 2019. 1
- [14] Ting Chen, Simon Kornblith, Mohammad Norouzi, and Geoffrey Hinton. A simple framework for contrastive learning of visual representations. In *International conference on machine learning*, pages 1597–1607. PMLR, 2020. 4, 7
- [15] Xinlei Chen, Haoqi Fan, Ross Girshick, and Kaiming He. Improved baselines with momentum contrastive learning. *arXiv preprint arXiv:2003.04297*, 2020. 2
- [16] Yezhen Cong, Samar Khanna, Chenlin Meng, Patrick Liu, Erik Rozi, Yutong He, Marshall Burke, David Lobell, and Stefano Ermon. Satmae: Pre-training transformers for temporal and multi-spectral satellite imagery. *Advances in Neural Information Processing Systems*, 35:197–211, 2022. 4, 11
- [17] Jon Dewitz and U.S. Geological Survey. National Land Cover Database (NLCD) 2019 products (ver. 2.0). U.S. Geological Survey data release, 2021. 6
- [18] Alexey Dosovitskiy, Lucas Beyer, Alexander Kolesnikov, Dirk Weissenborn, Xiaohua Zhai, Thomas Unterthiner, Mostafa Dehghani, Matthias Minderer, Georg Heigold, Sylvain Gelly, et al. An image is worth 16x16 words: Transformers for image recognition at scale. *arXiv preprint arXiv:2010.11929*, 2020. 7
- [19] Martin Hermann Paul Fuchs and Begüm Demir. Hyspecnet-11k: A large-scale hyperspectral dataset for benchmarking learning-based hyperspectral image compression methods. *arXiv preprint arXiv:2306.00385*, 2023. 2, 3, 4
- [20] Anthony Fuller, Koreen Millard, and James Green. Croma: Remote sensing representations with contrastive radar-optical masked autoencoders. *Advances in Neural Information Processing Systems*, 36, 2024. 4
- [21] Spyros Gidaris, Praveer Singh, and Nikos Komodakis. Unsupervised representation learning by predicting image rotations. In *ICLR 2018*, 2018. 3
- [22] Jean-Bastien Grill, Florian Strub, Florent Altché, Corentin Tallec, Pierre Richemond, Elena Buchatskaya, Carl Doersch, Bernardo Avila Pires, Zhaohan Guo, Mohammad Gheshlaghi Azar, et al.

- Bootstrap your own latent—a new approach to self-supervised learning. *Advances in neural information processing systems*, 33:21271–21284, 2020. 4, 8
- [23] Boran Han, Shuai Zhang, Xingjian Shi, and Markus Reichstein. Bridging remote sensors with multisensor geospatial foundation models, 2024. 4
- [24] Kaiming He, Xiangyu Zhang, Shaoqing Ren, and Jian Sun. Deep residual learning for image recognition. In *Proceedings of the IEEE conference on computer vision and pattern recognition*, pages 770–778, 2016. 7
- [25] Kaiming He, Ross Girshick, and Piotr Dollár. Rethinking imagenet pre-training. In *Proceedings of the IEEE/CVF International Conference on Computer Vision*, pages 4918–4927, 2019. 9
- [26] Kaiming He, Haoqi Fan, Yuxin Wu, Saining Xie, and Ross Girshick. Momentum contrast for unsupervised visual representation learning. In *Proceedings of the IEEE/CVF conference on computer vision and pattern recognition*, pages 9729–9738, 2020. 2, 4, 7, 8, 9, 10
- [27] Kaiming He, Xinlei Chen, Saining Xie, Yanghao Li, Piotr Dollár, and Ross Girshick. Masked autoencoders are scalable vision learners. In *Proceedings of the IEEE/CVF conference on computer vision and pattern recognition*, pages 16000–16009, 2022. 2, 4, 7, 9, 12
- [28] Danfeng Hong, Lianru Gao, Jing Yao, Bing Zhang, Antonio Plaza, and Jocelyn Chanussot. Graph convolutional networks for hyperspectral image classification. *IEEE Transactions on Geoscience and Remote Sensing*, 59(7):5966–5978, 2020. 7
- [29] Danfeng Hong, Zhu Han, Jing Yao, Lianru Gao, Bing Zhang, Antonio Plaza, and Jocelyn Chanussot. Spectralformer: Rethinking hyperspectral image classification with transformers. *IEEE Transactions on Geoscience and Remote Sensing*, 60:1–15, 2021. 7
- [30] Danfeng Hong, Bing Zhang, Hao Li, Yuxuan Li, Jing Yao, Chenyu Li, Martin Werner, Jocelyn Chanussot, Alexander Zipf, and Xiao Xiang Zhu. Cross-city matters: A multimodal remote sensing benchmark dataset for cross-city semantic segmentation using high-resolution domain adaptation networks. *Remote Sensing of Environment*, 299:113856, 2023. 2
- [31] Danfeng Hong, Bing Zhang, Xuyang Li, Yuxuan Li, Chenyu Li, Jing Yao, Naoto Yokoya, Hao Li, Pedram Ghamisi, Xiuping Jia, et al. Spectralgpt: Spectral remote sensing foundation model. *IEEE Transactions on Pattern Analysis and Machine Intelligence*, 2024. 4, 9
- [32] Sikang Hou, Hongye Shi, Xianghai Cao, Xiaohua Zhang, and Licheng Jiao. Hyperspectral imagery classification based on contrastive learning. *IEEE Transactions on Geoscience and Remote Sensing*, 60:1–13, 2021. 4
- [33] Damian Ibanez, Ruben Fernandez-Beltran, Filiberto Pla, and Naoto Yokoya. Masked auto-encoding spectral–spatial transformer for hyperspectral image classification. *IEEE Transactions on Geoscience and Remote Sensing*, 60:1–14, 2022. 4
- [34] Johannes Jakubik, Sujit Roy, C. E. Phillips, Paolo Fraccaro, Denys Godwin, Bianca Zadrozny, Daniela Szwarcman, Carlos Gomes, Gabby Nyirjesy, Blair Edwards, Daiki Kimura, Naomi Simumba, Linsong Chu, S. Karthik Mukkavilli, Devyani Lambhate, Kamal Das, Ranjini Bangalore, Dario Oliveira, Michal Muszynski, Kumar Ankur, Muthukumaran Ramasubramanian, Iksha Gurung, Sam Khallaghi, Hanxi Li, Michael Cecil, Maryam Ahmadi, Fatemeh Kordi, Hamed Alemohammad, Manil Maskey, Raghu Ganti, Kommy Weldemariam, and Rahul Ramachandran. Foundation models for generalist geospatial artificial intelligence, 2023. 6, 9, 11
- [35] Jianxin Jia, Yueming Wang, Jinsong Chen, Ran Guo, Rong Shu, and Jianyu Wang. Status and application of advanced airborne hyperspectral imaging technology: A review. *Infrared Physics & Technology*, 104:103115, 2020. 1
- [36] Longlong Jing and Yingli Tian. Self-supervised visual feature learning with deep neural networks: A survey. *IEEE transactions on pattern analysis and machine intelligence*, 43(11):4037–4058, 2020. 3
- [37] Hermann Kaufmann, S Förster, Hendrik Wulf, K Segl, Luis Guanter, M Bochow, U Heiden, A Müller, W Heldens, T Schneiderhan, et al. Science plan of the environmental mapping and analysis program (enmap). 2012. 1, 5
- [38] G Kerr, Janja Avbelj, Emiliano Carmona, Andreas Eckardt, Birgit Gerasch, Lewis Graham, Burghardt Günther, Uta Heiden, David Krutz, Harald Krawczyk, et al. The hyperspectral sensor desis on muses: Processing and applications. In *2016 IEEE International Geoscience and Remote Sensing Symposium (IGARSS)*, pages 268–271. IEEE, 2016. 1
- [39] Muhammad Jaleed Khan, Hamid Saeed Khan, Adeel Yousaf, Khurram Khurshid, and Asad Abbas. Modern trends in hyperspectral image analysis: A review. *Ieee Access*, 6:14118–14129, 2018. 1
- [40] Yoonho Lee, Annie S Chen, Fahim Tajwar, Ananya Kumar, Huaxiu Yao, Percy Liang, and Chelsea Finn. Surgical fine-tuning improves adaptation to distribution shifts. *arXiv preprint arXiv:2210.11466*, 2022. 8
- [41] Johannes Lehner, Benedikt Alkin, Andreas Fürst, Elisabeth Rumetshofer, Lukas Miklautz, and Sepp Hochreiter. Contrastive tuning: A little help to make masked autoencoders forget. *arXiv preprint arXiv:2304.10520*, 2023. 8

- [42] Xuyang Li, Danfeng Hong, and Jocelyn Chanut. S2mae: A spatial-spectral pretraining foundation model for spectral remote sensing data. In *Proceedings of the IEEE/CVF Conference on Computer Vision and Pattern Recognition*, pages 24088–24097, 2024. 4
- [43] Zhaokui Li, Hui Guo, Yushi Chen, Cuiwei Liu, Qian Du, Zhuoqun Fang, and Yan Wang. Few-shot hyperspectral image classification with self-supervised learning. *IEEE Transactions on Geoscience and Remote Sensing*, 61:1–17, 2023. 4
- [44] Weiwei Liu, Kai Liu, Weiwei Sun, Gang Yang, Kai Ren, Xiangchao Meng, and Jiangtao Peng. Self-supervised feature learning based on spectral masking for hyperspectral image classification. *IEEE Transactions on Geoscience and Remote Sensing*, 2023. 4
- [45] Bing Lu, Phuong D Dao, Jianguo Liu, Yuhong He, and Jiali Shang. Recent advances of hyperspectral imaging technology and applications in agriculture. *Remote Sensing*, 12(16):2659, 2020. 1
- [46] Oscar Manas, Alexandre Lacoste, Xavier Giró-i Nieto, David Vazquez, and Pau Rodriguez. Seasonal contrast: Unsupervised pre-training from uncurated remote sensing data. In *Proceedings of the IEEE/CVF International Conference on Computer Vision*, pages 9414–9423, 2021. 4, 5, 11
- [47] Matias Mendieta, Boran Han, Xingjian Shi, Yi Zhu, Chen Chen, and Mu Li. Gfm: Building geospatial foundation models via continual pretraining. *arXiv preprint arXiv:2302.04476*, 2023. 4
- [48] Ishan Misra and Laurens van der Maaten. Self-supervised learning of pretext-invariant representations. In *Proceedings of the IEEE/CVF conference on computer vision and pattern recognition*, pages 6707–6717, 2020. 3
- [49] Jakub Nalepa, Bertrand Le Saux, Nicolas Longépé, Lukasz Tulczyjew, Michal Myller, Michal Kawulok, Krzysztof Smykala, and Michal Gumiela. The hyperview challenge: Estimating soil parameters from hyperspectral images. In *2022 IEEE International Conference on Image Processing (ICIP)*, pages 4268–4272. IEEE, 2022. 2, 8
- [50] Alejandro Newell and Jia Deng. How useful is self-supervised pretraining for visual tasks? In *Proceedings of the IEEE/CVF Conference on Computer Vision and Pattern Recognition*, pages 7345–7354, 2020. 10
- [51] Maxime Oquab, Timothée Darcet, Théo Moutakanni, Huy Vo, Marc Szafraniec, Vasil Khalidov, Pierre Fernandez, Daniel Haziza, Francisco Massa, Alaaeldin El-Nouby, et al. Dinov2: Learning robust visual features without supervision. *arXiv preprint arXiv:2304.07193*, 2023. 2, 7, 8, 9, 10
- [52] Stefano Pignatti, Angelo Palombo, Simone Pascucci, Filomena Romano, Federico Santini, Tiziana Simonello, Amato Umberto, Cuomo Vincenzo, Nicola Acito, Marco Diani, et al. The prisma hyperspectral mission: Science activities and opportunities for agriculture and land monitoring. In *2013 IEEE International Geoscience and Remote Sensing Symposium-IGARSS*, pages 4558–4561. IEEE, 2013. 1
- [53] Michael Rast, Jens Nieke, J Adams, Claudia Isola, and Ferran Gascon. Copernicus hyperspectral imaging mission for the environment (chime). In *2021 IEEE International Geoscience and Remote Sensing Symposium IGARSS*, pages 108–111. IEEE, 2021. 1, 5
- [54] Colorado J Reed, Ritwik Gupta, Shufan Li, Sarah Brockman, Christopher Funk, Brian Clipp, Kurt Keutzer, Salvatore Candido, Matt Uyttendaele, and Trevor Darrell. Scale-mae: A scale-aware masked autoencoder for multiscale geospatial representation learning. In *Proceedings of the IEEE/CVF International Conference on Computer Vision*, pages 4088–4099, 2023. 4
- [55] Linus Scheibenreif, Michael Mommert, and Damian Borth. Masked vision transformers for hyperspectral image classification. In *Proceedings of the IEEE/CVF Conference on Computer Vision and Pattern Recognition*, pages 2165–2175, 2023. 2, 3, 4
- [56] Adam Stewart, Nils Lehmann, Isaac Corley, Yi Wang, Yi-Chia Chang, Nassim Ait Ali Braham, Shradha Sehgal, Caleb Robinson, and Arindam Banerjee. Ssl4eo-1: Datasets and foundation models for landsat imagery. *Advances in Neural Information Processing Systems*, 36, 2024. 4, 6, 11
- [57] Gencer Sumbul, Marcela Charfuelan, Begüm Demir, and Volker Markl. Bigearthnet: A large-scale benchmark archive for remote sensing image understanding. In *IGARSS 2019-2019 IEEE International Geoscience and Remote Sensing Symposium*, pages 5901–5904. IEEE, 2019. 6
- [58] Gencer Sumbul, Arne De Wall, Tristan Kreuziger, Filipe Marcelino, Hugo Costa, Pedro Benevides, Mario Caetano, Begüm Demir, and Volker Markl. Bigearthnet-mm: A large-scale, multimodal, multi-label benchmark archive for remote sensing image classification and retrieval [software and data sets]. *IEEE Geoscience and Remote Sensing Magazine*, 9(3):174–180, 2021. 6
- [59] Rui Tian, Danqing Liu, Yu Bai, Yu Jin, Guanliang Wan, and Yanhui Guo. Swin-msp: A shifted windows masked spectral pretraining model for hyperspectral image classification. *IEEE Transactions on Geoscience and Remote Sensing*, 2024. 4
- [60] University of the Basque Country. Hyperspectral remote sensing scenes, Accessed in 2023. [Online; accessed in 2023]. 2, 4

- [61] Vipin Upadhyay and Amit Kumar. Hyperspectral remote sensing of forests: technological advancements, opportunities and challenges. *Earth Science Informatics*, 11:487–524, 2018. [1](#)
- [62] Freek D Van der Meer, Harald MA Van der Werff, Frank JA Van Ruitenbeek, Chris A Hecker, Wim H Bakker, Marleen F Noomen, Mark Van Der Meijde, E John M Carranza, J Boudewijn De Smeth, and Tsehaie Woldai. Multi-and hyperspectral geologic remote sensing: A review. *International Journal of Applied Earth Observation and Geoinformation*, 14(1):112–128, 2012. [1](#)
- [63] Di Wang, Meiqi Hu, Yao Jin, Yuchun Miao, Jiaqi Yang, Yichu Xu, Xiaolei Qin, Jiaqi Ma, Lingyu Sun, Chenxing Li, Chuan Fu, Hongruixuan Chen, Chengxi Han, Naoto Yokoya, Jing Zhang, Minqiang Xu, Lin Liu, Lefei Zhang, Chen Wu, Bo Du, Dacheng Tao, and Liangpei Zhang. Hypersigma: Hyperspectral intelligence comprehension foundation model, 2024. [2](#), [3](#), [4](#), [10](#), [11](#)
- [64] Yi Wang, Conrad Albrecht, Nassim Ait Ali Braham, Lichao Mou, and Xiaoxiang Zhu. Self-supervised learning in remote sensing: A review. *IEEE Geoscience and Remote Sensing Magazine*, 2022. [2](#)
- [65] Yi Wang, Nassim Ait Ali Braham, Zhitong Xiong, Chenying Liu, Conrad M Albrecht, and Xiao Xiang Zhu. Ssl4eo-s12: A large-scale multi-modal, multi-temporal dataset for self-supervised learning in earth observation. *arXiv preprint arXiv:2211.07044*, 2022. [4](#), [5](#), [11](#)
- [66] Yue Wang, Ming Wen, Hailiang Zhang, Jinyu Sun, Qiong Yang, Zhimin Zhang, and Hongmei Lu. Hsi-mae: A unified masked autoencoder with large-scale pre-training for hyperspectral image classification. *IEEE Journal of Selected Topics in Applied Earth Observations and Remote Sensing*, 2024. [4](#)
- [67] Yiqun Xie, Zhihao Wang, Weiye Chen, Zhili Li, Xiaowei Jia, Yanhua Li, Ruichen Wang, Kangyang Chai, Ruohan Li, and Sergii Skakun. When are foundation models effective? understanding the suitability for pixel-level classification using multispectral imagery. *arXiv preprint arXiv:2404.11797*, 2024. [11](#)
- [68] Zhenda Xie, Zheng Zhang, Yue Cao, Yutong Lin, Jianmin Bao, Zhuliang Yao, Qi Dai, and Han Hu. Simmim: A simple framework for masked image modeling. In *Proceedings of the IEEE/CVF Conference on Computer Vision and Pattern Recognition*, pages 9653–9663, 2022. [4](#)
- [69] Zhitong Xiong, Yi Wang, Fahong Zhang, Adam J Stewart, Joëlle Hanna, Damian Borth, Ioannis Papoutsis, Bertrand Le Saux, Gustau Camps-Valls, and Xiao Xiang Zhu. Neural plasticity-inspired foundation model for observing the earth crossing modalities. *arXiv preprint arXiv:2403.15356*, 2024. [11](#)
- [70] Jure Zbontar, Li Jing, Ishan Misra, Yann LeCun, and Stéphane Deny. Barlow twins: Self-supervised learning via redundancy reduction. In *International Conference on Machine Learning*, pages 12310–12320. PMLR, 2021. [4](#)
- [71] Richard Zhang, Phillip Isola, and Alexei A Efros. Colorful image colorization. In *Computer Vision—ECCV 2016: 14th European Conference, Amsterdam, The Netherlands, October 11–14, 2016, Proceedings, Part III 14*, pages 649–666. Springer, 2016. [3](#)
- [72] Zilong Zhong, Jonathan Li, Zhiming Luo, and Michael Chapman. Spectral–spatial residual network for hyperspectral image classification: A 3-d deep learning framework. *IEEE Transactions on Geoscience and Remote Sensing*, 56(2):847–858, 2017. [7](#)

# SpectralEarth: Training Hyperspectral Foundation Models at Scale

## Supplementary Material

### 8. Implementation Details

#### 8.1. Network Architecture

**Spectral Adapter.** The Spectral Adapter consists of three (1D Conv + BN + ReLu) layers. The kernel sizes for the 1D convolutions are 7, 7, and 5, with strides of 5, 5, and 3, respectively. The resulting feature maps have 128 channels. To accommodate different sensors and feed the input into standard 2D backbones, we use a global pooling layer to aggregate the remaining spectral dimensions (if any).

**Spec. RN50.** The architecture of Spec. RN50 closely follows the classical ResNet-50 design with two modifications: (a) We replace the stem layers with the spectral adapter without downscaling; (b) The first bottleneck block is adjusted to take an input feature map of 128 channels, as opposed to the ResNet-50’s 64-channel input at this stage.

**Spec. ViT-S.** For Spec. ViT-S, we set the number of input channels in the projection layer to 128. A patch size of 4 is chosen based on two considerations: (a) to preserve the rich spectral information in hyperspectral tokens without excessive compression in the patch projection layer, and (b) to preserve fine-grained details spatially while keeping a reasonable compute cost given the small image size of 128x128.

#### 8.2. Training Details

Detailed training configurations and hyperparameters for each downstream task are presented below. For each experiment, a search over the learning rate was performed.

**Multi-label Classification** For multi-label classification, we utilized the Binary Cross-Entropy (BCE) loss function. Training was conducted over 100 epochs with a batch size of 128. AdamW optimizer was employed with a cosine annealing scheduler. Data augmentation included random resized crop, horizontal and vertical flipping.

**Semantic Segmentation** Training was conducted for 100 epochs on all datasets, using a Cross-Entropy loss. AdamW optimizer was used with a batch size of 64 for EnMAP-NLCD and 32 for EnMAP-CDL and DESIS-CDL. We used a cosine annealing scheduler. Data augmentation included random resized crop, horizontal and vertical flipping.

**Regression** We resized all images in the Hyperview dataset to 128x128 pixels. We trained for 200 epochs with a normalized mean squared error (MSE) loss function, as described in Section 5.4. The AdamW optimizer was used along with a cosine annealing scheduler and a batch size of 16. As for the other tasks, we used random resized crop, horizontal and vertical flipping during training.

### 9. Data Visualizations

In this section, we provide additional data visualizations to get deeper insights into the characteristics of SpectralEarth, as well as hyperspectral EnMAP imagery. Samples of EnMAP tiles, i.e. before division into patches and the filtering of water absorption bands, used to create our dataset are displayed in Figure 15.

#### 9.1. Spectral Reflectance Analysis

To gain more insights into the spectral characteristics in our dataset, we present an analysis of per-class spectral reflectance for the NLCD task, visualized in Figure 16.

The spectral reflectance profiles across different land cover classes show diverse characteristics. Classes such as ‘Open Water’ and ‘Barren Land’ have distinct spectral signatures that are characteristic of their respective land cover types. Conversely, some classes, such as ‘Deciduous Forest’ and ‘Evergreen Forest’, have profiles that are harder to differentiate from one another. This inter-class similarity poses challenges in classification tasks, highlighting the need for advanced feature extractors capable of capturing such subtle differences.

Furthermore, Figure 16 reveals a high level of intra-class spectral variability, a well-known characteristic of hyperspectral imagery. This variance reflects the diverse nature of each land cover class, influenced by factors such as illumination conditions and seasonal changes. This emphasizes the need for robust models to ensure reliable performance across different geographic regions and environmental conditions.

#### 9.2. Temporal Analysis

We analyze the temporal coverage of our dataset in Figure 17. SpectralEarth includes data from all seasons, with a relatively balanced distribution across months. However, certain disparities can be observed, e.g., January is underrepresented while July, August, and March are overrepresented. This can be attributed to several factors: (a) Increased cloud cover during winter months, which inherently limits the availability of clear imagery; (b) A satellite

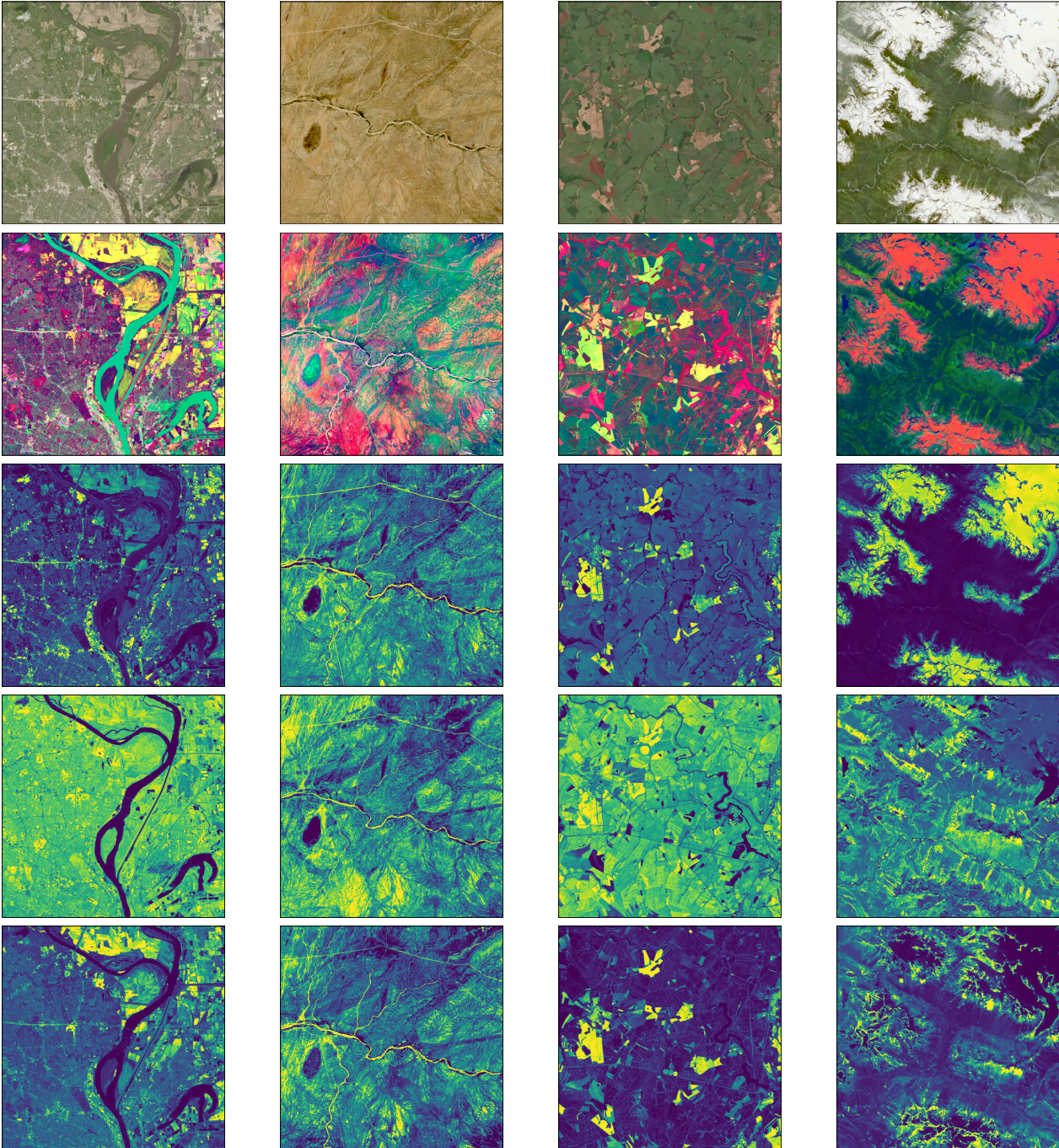


Figure 15. Sample visualizations of EnMAP tiles used to create the SpectralEarth dataset depicting RGB composites (first row), false color PCA composites (second row), and reflectance values for bands 20 (third row), 120 (fourth row) and 220 (fifth row). These representations highlight the rich information carried in the spectral bands. Notably, each band accentuates distinct features of the terrain.

outage in **December-January 2023** and **December-January 2024**, which resulted in a temporary interruption of data acquisition; (c) The task scheduling nature of the EnMAP mission. As EnMAP is operationally tasked based on specific use cases, the distribution of data inherently reflects the

real-world demands of satellite imagery, leading to a natural variation in seasonal coverage.

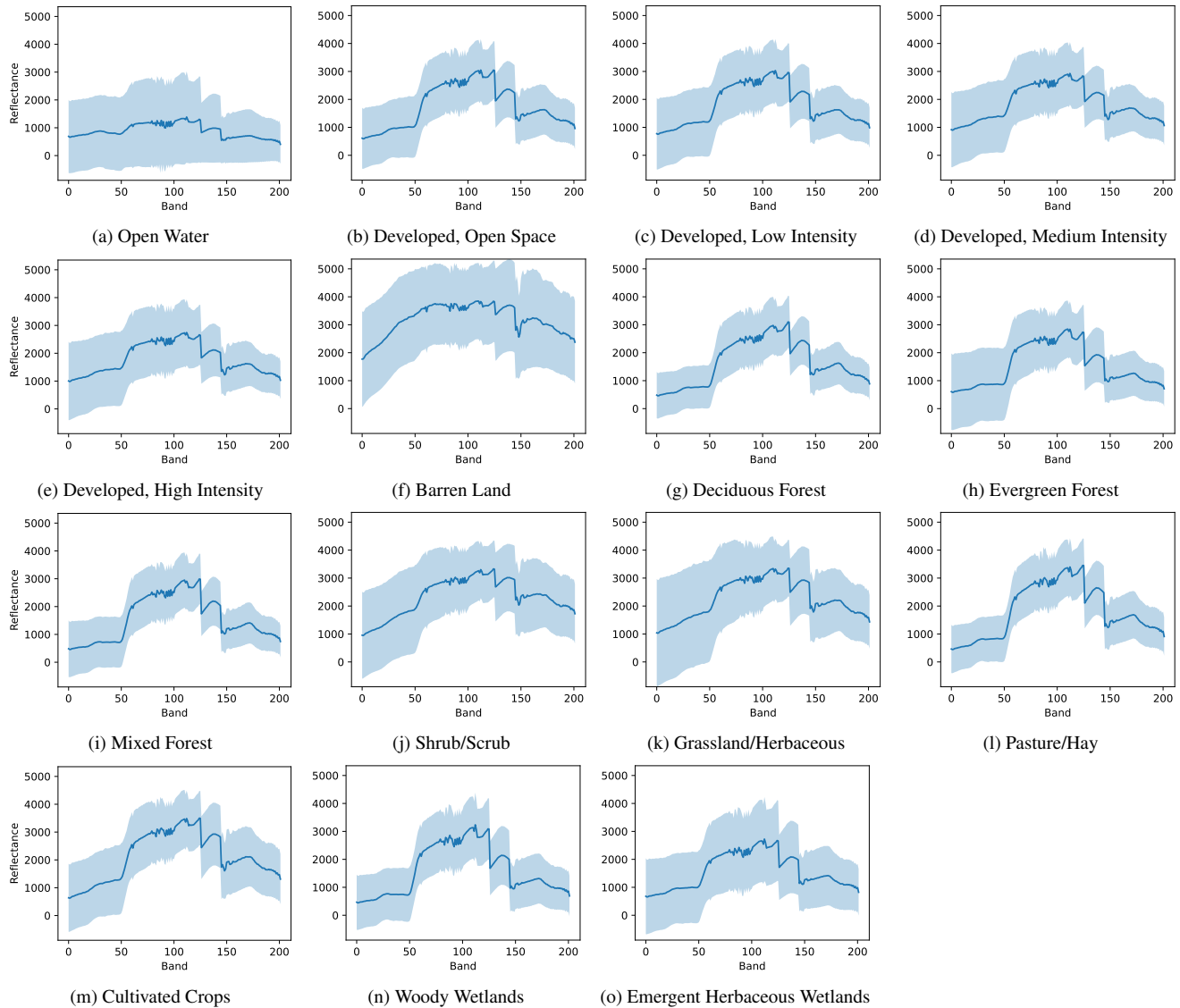


Figure 16. Mean spectral reflectance per class in the EnMAP-NLCD dataset.

### 9.3. Class Distribution in Downstream Tasks

**EnMAP-CORINE** The EnMAP-CORINE dataset exhibits a diverse range of land cover types. As Figure 18 demonstrates, some classes such as 'Arable Land' and 'Complex cultivation patterns' are more frequent, while others like 'Coastal/Inland wetlands' and 'Beaches, dunes, sand' are comparatively rare. This class imbalance reflects the natural land cover distribution in Europe.

**EnMAP-CDL** The EnMAP-CDL dataset is primarily focused on agricultural crop types. However, following the CDL map, the dataset also includes some non-agricultural classes such as grassland, which is over-represented as shown in Figure 19. Overall, the dataset exhibits a reason-

able level of class balance among the different crop types.

**EnMAP-NLCD** The EnMAP-NLCD dataset provides a comprehensive view of natural and urban land covers. As depicted in Figure 20, albeit some infrequent classes like 'Developed, High Intensity', the class distribution is well-balanced.

**DESIS-CDL** Similar to the EnMAP-CDL dataset, DESIS-CDL is focused on agricultural classes. Due to the limited availability of DESIS tiles, it was not possible to pair this dataset with EnMAP-CDL. Therefore, the class distribution (see Figure 21) and geographical coverage differ.

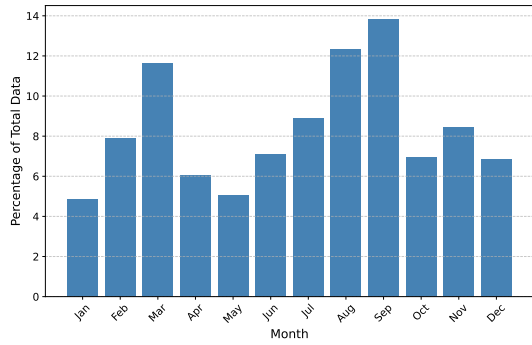


Figure 17. SpectralEarth temporal distribution by month.

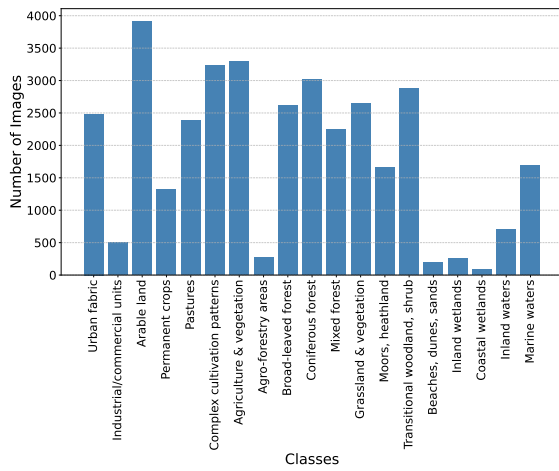


Figure 18. Class distribution of the EnMAP-CORINE dataset.

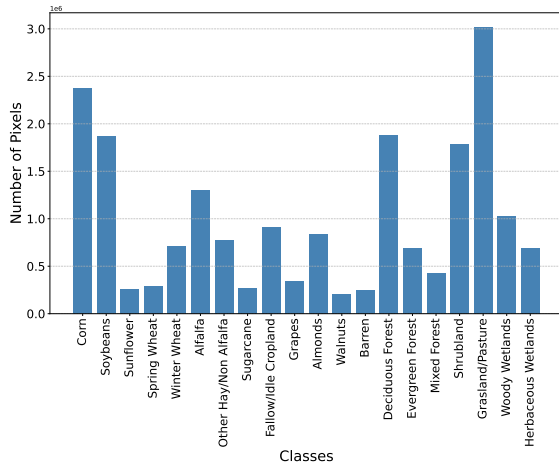


Figure 19. Class distribution of the EnMAP-CDL dataset.

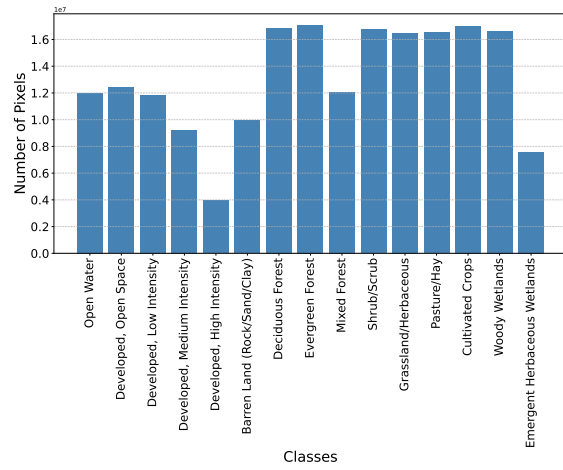


Figure 20. Class distribution in the EnMAP-NLCD dataset.

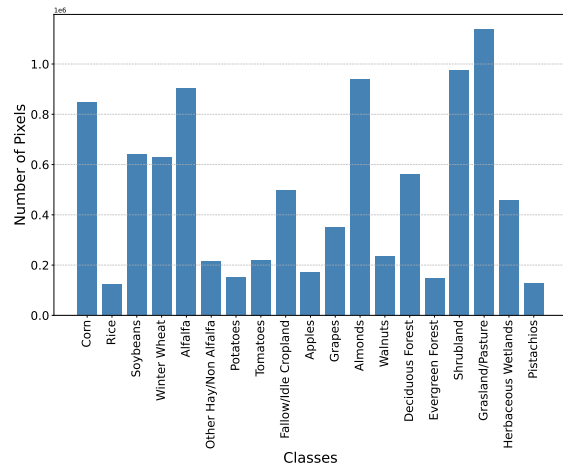


Figure 21. Class distribution in the DESIS-CDL dataset.